ARTICLE

Check for updates

Barnacle cement protein as an efficient bioinspired corrosion inhibitor

My Hanh Bui[1,5], Shu Hui Hiew[1,5], Teddy Salim [2], Wan Geok Saw [3], Richard D. Webster [4], Gerhard Grüber[3], Yuguang Mu [3] & Ali Miserez [1,2,3✉]

To prevent corrosion damage in aggressive environments such as seawater, metallic surfaces are coated with corrosion inhibitors usually made of organic molecules. Unfortunately, these inhibitors often exhibit environmental toxicity and are hazardous to natural habitats. Thus, developing greener and effective corrosion inhibitors is desirable. Here, we present an alternative green inhibitor, the recombinant protein rMrCP20 derived from the adhesive cement of the barnacle *Megabalanus rosa* and show that it efficiently protects mild steel against corrosion under high salt conditions mimicking the marine environment. We reveal that these anti-corrosion properties are linked to the protein's biophysical properties, namely its strong adsorption to surfaces combined with its interaction with Fe ions released by steel substrates, which forms a stable layer that increases the coating's impedance and delays corrosion. Our findings highlight the synergistic action of rMrCP20 in preventing corrosion and provide molecular-level guidelines to develop alternative green corrosion inhibitor additives.

[1] Center for Sustainable Materials (SusMat), School of Materials Science and Engineering, Nanyang Technological University, Singapore 639798, Singapore. [2] School of Materials Science and Engineering, Nanyang Technological University, Singapore 639798, Singapore. [3] School of Biological Sciences, Nanyang Technological University, Singapore 637551, Singapore. [4] School of Chemistry, Chemical Engineering and Biotechnology, Nanyang Technological University, Singapore 637371, Singapore. [5] These authors contributed equally: My Hanh Bui, Shu Hui Hiew. ✉email: ali.miserez@ntu.edu.sg

Corrosion damage is a ubiquitous issue for metallic structures submerged in the sea, as the high-salt environment causes surface material erosion and crevice corrosion by dissolution of the metal ions during complex electrochemical and anaerobic corrosion processes[1–3]. The calculated rates of steel corrosion below sea level are between 0.08–0.14 mm yr^{-1} and 0.07–0.21 mm yr^{-1} in splash and tidal zones[3], while the global cost of corrosion is estimated to be *ca.* US$2.5 trillion per year in 2013[4]. The useful lifespan of metals becomes significantly reduced when exposed to saltwater, requiring frequent maintenance, which is especially costly for petroleum, offshore construction and sea transport industries. By implementing existing anti-corrosion protection methods, the cost could be reduced by 15–35%, or as much as US$875 billion annually[4]. Among these strategies, the addition of chemical compounds to the medium in contact with the surface, called corrosion inhibitors, is one of the most convenient methods to reduce the corrosion rate of steels. Most efficient commercially-used inhibitors are organic compounds, such as azole derivatives[5,6], Schiff bases[7–9], phenolic compounds[3], amine derivatives[10,11], thio-compounds[11,12] and pyrimidine derivatives[11,13]. These inhibitors usually contain electronegative atoms, heterocyclic compounds containing polar functional groups and conjugated double bonds in their molecular structures[14], through which they absorb on metal surfaces by forming an adhesive film that restricts the exposure of the metal to corrosive media. Although these synthetic compounds exhibit good corrosion inhibition performance, they bring concerns with regard to how they may affect living organisms[15]. Thus, there is a strong push to develop bio-based corrosion inhibitors that are chemically and mechanically robust but do not release non-natural organic chemicals into the environment.

Protein and its amino acids are compounds that contain amino and carboxyl groups gathering as a feature of their molecular structure. This unique structure proposes that they would be potential applicants as corrosion inhibitors[16]. In fact, amino acids have been systematically researched as corrosion inhibitors in corrosive media to control the inhibition of corrosion reactions of metals[16–18]. Of note, mussel adhesive protein (Mefp-1) derived from the marine mussel *Mytilus edulis* has been shown to exhibit good corrosion inhibition on carbon steel[19–22].

Here, we report our findings on the anti-corrosion properties of a recombinant protein, rMrCP20, derived from the natural adhesive cement protein (MrCP20) of a common marine biofouler, the barnacle *Megabalanus rosa* (*M. rosa*). Barnacles are sessile crustaceans that strongly adhere to solid immersed substrates. Blackwood et al.[23] and Eashwar et al.[24] have reported that barnacle attachment to stainless steel substrates in seawater leads to more substantial corrosion events under dead barnacles, while crevice corrosion of steel substrates underneath live barnacles was less than 4%. Barnacles have been demonstrated to adhere strongly to metal substrates[25] and to minimize corrosion events in such conditions of strong attachment. Hence, drawing inspiration from the structural adaptation of *M. rosa* and these reported observations, we posited that the adhesive protein MrCP20 may help prevent steel corrosion provided it binds strongly to the substrate. Our team has previously unveiled the secondary and tertiary structures of rMrCP20[26] and identified that its underwater adhesive properties stem from its high content of cysteines (Cys) and charged amino acid residues.

Herein, we show that rMrCP20 protein exhibits concentration-dependent anti-corrosion properties, which as we demonstrate is linked to its adhesive characteristics in conjunction with its ability to capture Fe ions released from the steel surface. Corrosion inhibition effect of rMrCP20 was demonstrated through time-resolved observations of corrosion on the alloy – mild steel (AH36) coupon, whereas the iron weight loss from the corrosion

events was measured via inductively coupled plasma optical emission spectroscopy (ICP-OES). A series of electrochemical studies provided insights into the increased impedance, corrosion inhibition process and redox reactions of the protein, while small angle X-ray scattering (SAXS) confirmed the protein's oligomeric conformation at the optimal corrosion inhibition concentration. Quartz crystal microbalance with dissipation monitoring (QCM-D) and nanoindentation studies indicate that rMrCP20 strongly adhered to steel substrates, with the presence of Fe ions resulting in compaction of the nanoscale protein film. Fourier Transformed Infrared Spectroscopy (FTIR) in conjunction with molecular dynamics (MD) simulations identified the main molecular interactions between rMrCP20 and Fe ions, in particular indicating that Fe^{3+} ions form ionic bridges and coordination bonds with the negatively charged side chain and histidine (His) residues of rMrCP20, respectively. Finally, fluorescence microscopy of tagged rMrCP20 in conjunction with Auger electron spectroscopy (AES) and X-ray photoelectron spectroscopy (XPS) surface mapping indicated preferential adsorption of the protein at the grain boundary (GB) of the steel surface, which we suggest helps mitigating GBs-initiated corrosion.

Results and discussion

Anticorrosion studies. rMrCP20 was first expressed and purified using the same protocol as previously described[26]. To examine the corrosion-inhibition properties of rMrCP20 protein, epoxy-embedded polished AH36 steel coupons were immersed in a pH 8.3 buffer containing 150 mM NaCl and 20 mM Tris(hydroxymethyl)aminomethane (Tris), in the absence or presence of rMrCP20 at different concentrations (see Materials and Methods). Figure 1a, b illustrate representative pictures of AH36 coupons at various time points and their respective immersion solutions after 24 h, at a range of rMrCP20 concentrations from 0 to 10 mg mL^{-1}.

In the absence of rMrCP20, the coupons underwent corrosion, with surfaces covered with rust and other corrosion products, and the respective buffer solution turning into intense brown color. Pitting corrosion was observed at different sites of the coupon substrate within the first hour and propagated as the immersion time increased, with the confined environment beneath the initial corrosion products appearing to accelerate pitting. Figure 1c illustrates a deep pitting site imaged by scanning electron microscopy (SEM). At a low concentration of *ca.* 0.1 mg mL^{-1}, rMrCP20 was previously found to accelerate the corrosion of steel coupon surfaces[27]. However, at increasing concentration of rMrCP20, corrosion was reduced considerably and little to no corrosion was observed on coupons incubated in 5 mg mL^{-1} and 10 mg mL^{-1} of proteins (Fig. 1a). These pits did not propagate further as the immersion time increased and their respective post-incubation buffer solutions had a light brown color (Fig. 1b). Further analysis was performed using ImageJ software to estimate the corroded area and the results are shown in Fig. 1d. In the absence of rMrCP20, on average 91% of AH36 coupon surfaces was corroded after 24 h. However, at increasing protein concentration surface corrosion was reduced drastically, down to 2% at 10 mg mL^{-1}, thereby demonstrating a concentration-dependent corrosion inhibition effect of rMrCP20 on AH36 steel.

Weight loss measurements are routinely employed to evaluate the effectiveness of metal corrosion inhibitors[28]. Fe content from the incubation solutions and respective coupon surfaces were measured by ICP-OES to reflect the total weight loss for each sample at concentrations of rMrCP20 from 0.1 mg mL^{-1} to 10 mg mL^{-1}, and to calculate the inhibition efficiency using Eqs. (1) and (2)[29,30].

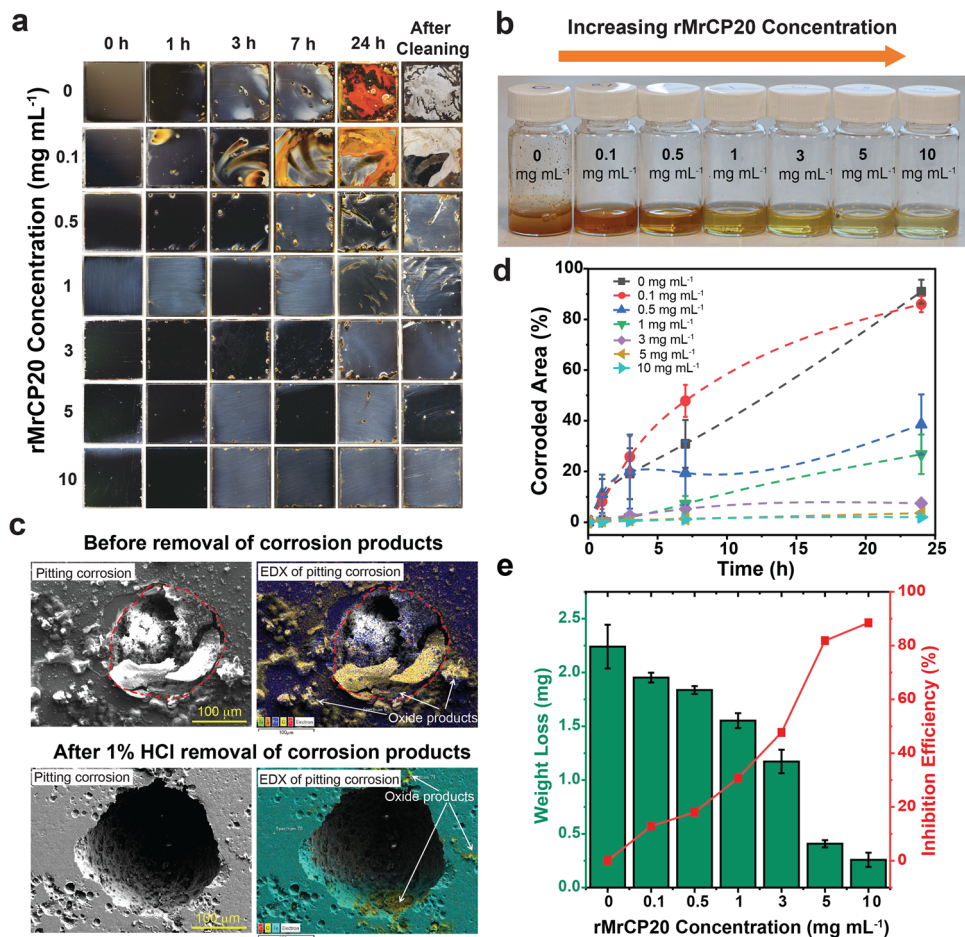$$CR = \frac{8.76 \times 10^4 \times \Delta m}{\rho AT} \qquad (1)$$

Fig. 1 Time-resolved study of corrosion on AH36 coupon. a Representative pictures of AH36 coupons showing the concentration-dependent anti-corrosion effect of *r*MrCP20 at immersion time intervals of 0, 1, 3, 7 and 24 h, and after cleaning the coupons with 1% HCl. **b** Respective buffer solutions after 24 h of coupon immersion. **c** Field emission scanning electron microscope (FESEM) images and overlay of energy dispersive X-ray spectroscopy (EDX) map of pitting corrosions before and after removal of corrosion products on surface of coupons, with a pitting of *ca.* 300 μm diameter outlined. **d** ImageJ analysis to determine percentage of corroded area of AH36 coupons. Error bars represent the standard error (SE) from triplicate tests. **e** Weight loss of AH36 over a 24 h incubation period and corresponding inhibition efficiency at increasing concentrations of *r*MrCP20. Error bars represent the SE from triplicate tests.

$$\eta\,(\%) = \theta \times 100 = \left(1 - \frac{CR_1}{CR_0}\right) \times 100 \qquad (2)$$

Where CR is the corrosion rate (mm yr^{-1}), Δm is the total weight loss (g), ρ is density of the metal samples (7.86 g cm^{-3}), A is the surface area (cm^2), and T is the exposure time (h). η is the corrosion inhibition efficiency (%), θ is the degree of surface coverage, while CR_0 and CR_1 are the weight losses of the coupons in the absence and presence of *r*MrCP20, respectively. The corrosion rate calculated via Eq. (1) decreased significantly with increasing the concentration of *r*MrCP20 (Supplementary Table 1), with the lowest corrosion rate of 0.12 mm yr^{-1} and a high corrosion-inhibition efficiency η of 88.48% (Fig. 1e). The observed enhanced corrosion-inhibition efficiency is attributed to the strong adhesive properties of *r*MrCP20, whereby protein adsorption to the coupon surfaces –and hence the degree of coupon surface coverage increased at higher protein concentrations.

Electrochemical studies. To further investigate the impedance brought about by different concentrations of *r*MrCP20, electro-chemical impedance spectroscopy (EIS) measurements were per-formed for AH36 samples after 24 h incubation in buffer solutions containing various concentrations of *r*MrCP20 protein. A protein concentration of 5 mg mL^{-1} was selected as the optimal con-centration for further characterizations as it exhibited good cor-rosion inhibition performance, whereas increasing the amount of protein to 10 mg mL^{-1} did not significantly affect the results.

Figure 2a–c show the Nyquist plots (Fig. 2a), Bode modulus (Fig. 2b) and phase angle representations (Fig. 2c) from EIS measurements. The Nyquist plots show single semi-circle loops from high to mid-frequency range, indicating that the corrosion of AH36 was controlled by a charge transfer process (Fig. 2a)[31–33]. Tailing was observed at the lower frequency range of each Nyquist plot, and these imperfections can be attributed to the roughness and heterogeneity of the AH36 working electrode[32,34], distribution of active center[34,35], adsorption of inhibitor molecules[36] and accumulation of corrosion products on the working electrode[35,36]. The diameter of the Nyquist plot is directly correlated to the impedance of the system, hence providing a suitable comparison of the resistance of the Fe substrate exposed to different concentrations of *r*MrCP20. The diameters increased at higher concentration of *r*MrCP20, suggesting that *r*MrCP20 adsorbed onto AH36 surfaces increases the charge transfer resistance and hence imparts corrosion resistance properties.

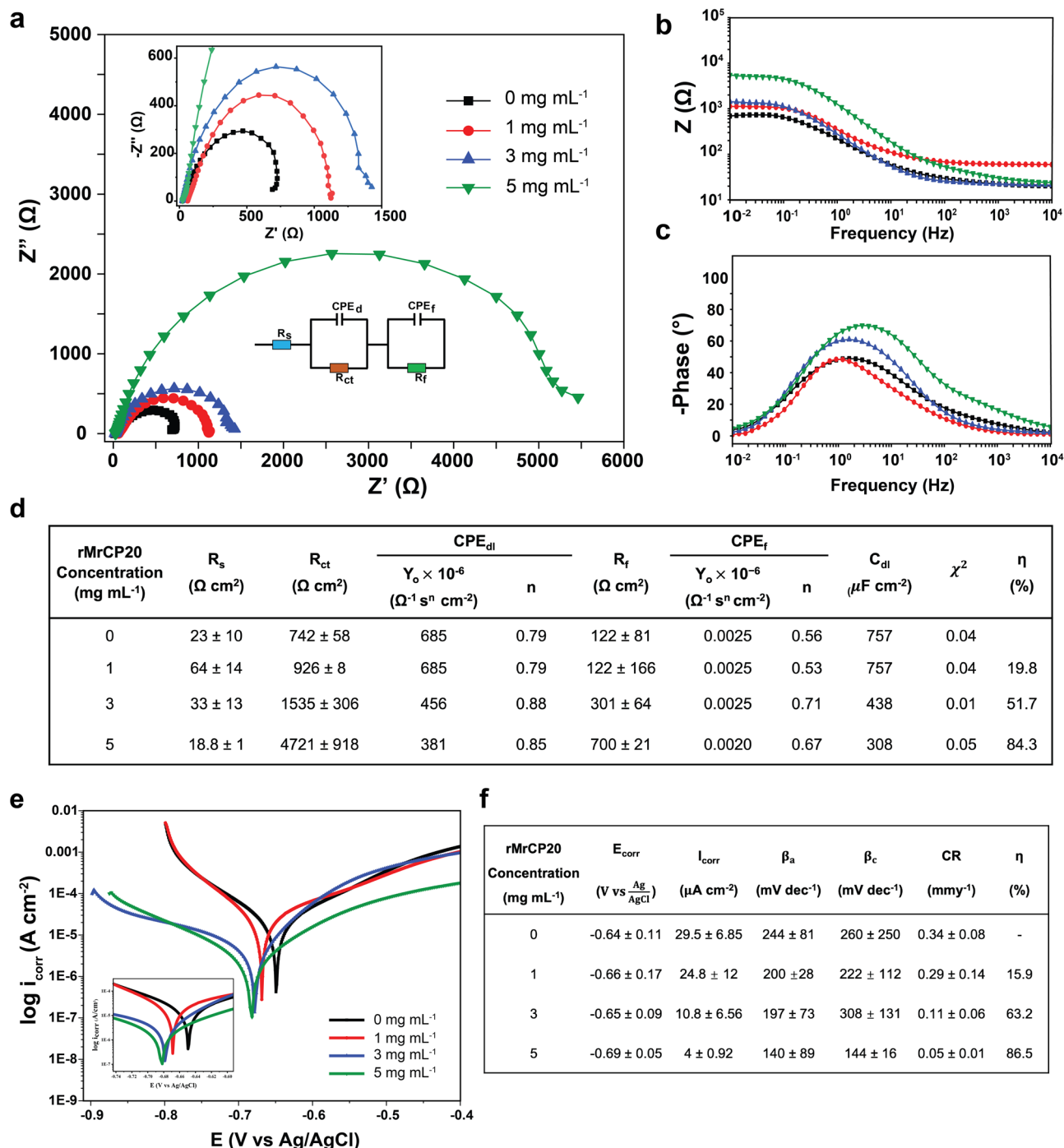**Fig. 2 Electrochemical impedance and potentiodynamic polarization (PDP) spectra after 24 h immersion. a** Nyquist plots with inset displaying the plots at higher frequencies between Z′ 0 to 1500 Ω and equivalent circuit diagram as inset. **b** Bode modulus plots. **c** Phase angle plots. **d** Summary table of electrochemical impedance parameters for AH36 in buffer solution, at various concentrations of rMrCP20 after 24 h immersion. Data are presented as average ± SE. **e** PDP curves in the potential range from −0.25 V versus OCP to −0.4 V versus Ag/AgCl with the sweep rate of 10 mV min^{-1} in aerated condition at 25 °C. The inset displays the plots in the range from −0.72 V to −0.60 V. **f** PDP parameters after 24 h immersion. Data are presented as average ± SE.

d

rMrCP20 Concentration (mg mL^{-1})	R_s (Ω cm^{-2})	R_{ct} (Ω cm^{-2})	CPE$_{dl}$ $Y_o \times 10^{-6}$ (Ω^{-1} s^n cm^{-2})	n	R_f (Ω cm^{-2})	CPE$_f$ $Y_o \times 10^{-6}$ (Ω^{-1} s^n cm^{-2})	n	C_{dl} (μF cm^{-2})	χ^2	η (%)
0	23 ± 10	742 ± 58	685	0.79	122 ± 81	0.0025	0.56	757	0.04	
1	64 ± 14	926 ± 8	685	0.79	122 ± 166	0.0025	0.53	757	0.04	19.8
3	33 ± 13	1535 ± 306	456	0.88	301 ± 64	0.0025	0.71	438	0.01	51.7
5	18.8 ± 1	4721 ± 918	381	0.85	700 ± 21	0.0020	0.67	308	0.05	84.3

f

rMrCP20 Concentration (mg mL^{-1})	E_{corr} (V vs $\frac{Ag}{AgCl}$)	I_{corr} (μA cm^{-2})	β_a (mV dec^{-1})	β_c (mV dec^{-1})	CR (mmy^{-1})	η (%)
0	−0.64 ± 0.11	29.5 ± 6.85	244 ± 81	260 ± 250	0.34 ± 0.08	-
1	−0.66 ± 0.17	24.8 ± 12	200 ± 28	222 ± 112	0.29 ± 0.14	15.9
3	−0.65 ± 0.09	10.8 ± 6.56	197 ± 73	308 ± 131	0.11 ± 0.06	63.2
5	−0.69 ± 0.05	4 ± 0.92	140 ± 89	144 ± 16	0.05 ± 0.01	86.5

Bode modulus plots (Fig. 2b) provide a more comprehensive representation of the impedance across the range of frequencies measured, while phase angle plots (Fig. 2c) indicate the phase shift across the range of frequencies and the plausible components in the respective equivalent electrical circuits (EEC). At higher protein concentrations, the Bode modulus plots show an increase in impedance values at low frequencies, where corrosion events are usually observed, while the phase angle plots

show an increase in the maximum phase angle value. The higher impedance is attributed to the formation of more homogenous rMrCP20 protein films at higher protein concentrations. Furthermore, the diameter of the Nyquist semicircles also increased with exposure time at higher rMrCP20 concentrations (Supplementary Fig. 1), which is caused by the formation of a mixed surface layer of corrosion products (iron oxide) and adsorbed proteins[36]. The evolution of the surface film most likely

involved complexation between rMrCP20 and Fe ions (Fe^{2+} and Fe^{3+}), which blocked the charge transfer path. This observation also highlights the stability of the adsorbed rMrCP20 molecules on the steel surface.

To further interpret the EIS results, an equivalent electrical circuit (EEC) model was chosen to extract the relevant electrochemical parameters (Fig. 2a inset). In the circuit, R_s represents the solution resistance, R_{ct} the charge transfer resistance, CPE_{dl} and CPE_f the constant phase elements of the double layer and protein film respectively, and R_f the resistance of the adsorbed rMrCP20 film. The double layer capacitance (C_{dl}) values were calculated from the expression[31]:

$$C_{dl} = \frac{Y_0 \omega^{n-1}}{\sin\left[n\left(\frac{\pi}{2}\right)\right]} \quad (3)$$

where Y_0 is the CPE constant, n is the CPE exponent, ω is the angular frequency ($\omega = 2\pi f_{max}$) in rad s^{-1}, and f_{max} is the frequency at which the imaginary component of the impedance is highest. The corrosion inhibition efficiency (% η) was calculated using Eq. (4)[37]:

$$\eta_{EIS}(\%) = \frac{R_{ct}^0 - R_{ct}'}{R_{ct}^0} \times 100 \quad (4)$$

where R_{ct}^0 and R_{ct}' are the charge transfer resistances in the presence and absence of rMrCP20, respectively. The values of the electrochemical parameters derived from the Nyquist plots are listed in Fig. 2d and demonstrate that adding rMrCP20 to the corrodent led to a reduction in C_{dl} and an increase in R_{ct} and R_f, which became more apparent as the rMrCP20 concentration increased. As the concentration of rMrCP20 increased from 1 to 5 mg mL^{-1}, the R_{ct} value increased from 926 Ω cm^2 to 4721 Ω cm^2, while the corresponding η value increased from 19.8% to 84.3%. The value of phase shift (n) for CPE_{dl} also increased from 0.79 without rMrCP20 to 0.85 in the presence of 5 mg mL^{-1} rMrCP20, suggesting a decrease in the heterogeneity of the coupon surface arising from adsorption of rMrCP20. C_{dl} for the control sample was 757 μF cm^{-2}, which was significantly higher than the corresponding value for the system incubated in rMrCP20, indicating growth in the electrical double layer thickness. These results suggest that the adsorption of rMrCP20 at the metal/electrolyte interface impedes charge transfer due to greater resistance. Hence, at higher concentration of rMrCP20, the AH36 steel surface is better protected against corrosion.

To obtain further qualitative understanding of the corrosion reactions, potentiodynamic polarization measurements (PDP) measurements were carried out on AH36 samples after 24 h incubation in the respective solutions, and the polarization curves are shown in Fig. 2e. The polarization curves present two opposing reactions, the anodic branch corresponding to Fe dissolution and the cathodic branch due to hydrogen evolution. The obtained polarization parameters, namely corrosion potential (E_{corr}), corrosion current density (i_{corr}), anodic and cathodic Tafel slopes (β_a and β_c) measured by the Tafel extrapolation method at the segment 20–50 mV from E_{corr} are presented in Fig. 2f. The corrosion rate (CR) and corrosion inhibition efficiency (η_{PDP}) of rMrCP20 was calculated using Eqs. (5) and (6)[37]:

$$\eta_{PDP}(\%) = \left(1 - \frac{i_{corr}^0}{i_{corr}'}\right) \times 100 \quad (5)$$

$$CR = 3.17E^{-9} \times \frac{M}{nF\rho A} i_{corr} \quad (6)$$

where i_{corr}^0 and i_{corr}' are the corrosion current densities in the presence and absence of rMrCP20, respectively, 3.17×10^{-9} is conversion factor, the ratio M/n is the equivalent weight, F

(96485 C mol^{-1}) is the Faraday constant, ρ (7.86 gcm^{-3}) is the density of the metal samples, and A is the area of the sample (cm^2). As shown in Fig. 2e, both the anodic and cathodic i_{corr} decreased in the presence of rMrCP20 and E_{corr} slightly shifted towards the cathodic direction, indicating that rMrCP20 has a stronger effect on the cathodic reaction than on the anodic reaction. This result was complemented with cyclic voltammetry (CV) measurements (Supplementary Fig. 2). Since the peaks of the redox reactions measured by CV were not shifted at different concentrations of rMrCP20, the reaction mechanism appeared to remain consistent. In addition, the peak currents observed in CV scans for both the oxidation and reduction reactions progressively decreased with the addition of rMrCP20, further confirming the lowered occurrence of redox reactions, and hence the corrosion inhibition properties of rMrCP20. Furthermore, the peak currents from CV measurements remained constant in the presence of rMrCP20 with repetitive scans, whereas in the absence of the protein the peak currents were much greater for the second scan.

As shown in Fig. 2f, i_{corr} decreased from 29.5 μA cm^{-2} without rMrCP20 down to 4.0 μA cm^{-2} with 5 mg mL^{-1} of rMrCP20. The lower values of i_{corr} in the presence of rMrCP20 can be attributed to protein adsorption onto the sample's surface and hence to the formation of a protective layer, which hinders the electron transfer process at the interface and reduces the rate of corrosion reactions. Figure 2f also illustrates the effect of rMrCP20 on the Tafel slopes values β_c, which were independent of the rMrCP20 concentration, indicating that the presence of rMrCP20 can suppress the corrosion process by blocking reaction sites without affecting the kinetics of the cathodic reactions[38]. Meanwhile, a gradual decline in β_a was observed with increasing rMrCP20 concentration, from 244 mV dec^{-1} in buffer to only 140 mV dec^{-1} in the presence of 5 mg mL^{-1} rMrCP20, indicating a change in the Fe dissolution mechanism. The change in Fe dissolution is attributed to the formation of metal-ion protein complexes as the protein interacts with the steel surface, which was further investigated by attenuated total reflection Fourier transform infrared spectroscopy (ATR-FTIR), QCM-D and MD simulations (discussed below). Accordingly, the corrosion-inhibition efficiency improved at increased rMrCP20 concentration, from 15.9% (1 mg mL^{-1}) to 86.5% (5 mg mL^{-1}), respectively. In summary, the corrosion inhibition values η obtained from all three methods (weight loss, EIS and PDP measurements) are consistent (Supplementary Fig. 3) and all indicate enhanced corrosion-inhibition activity as the concentration of rMrCP20 increased.

Adsorption of rMrCP20 and metal ion – protein interaction studies. QCM-D measurements were carried out on Fe sensors to examine the adsorption properties of rMrCP20, followed by subsequent addition of $FeCl_3$ analyte as a source of free Fe^{3+} to investigate the Fe^{3+}/adsorbed protein layer interactions. The changes in resonance frequency (Δf) and dissipation (ΔD) of the sensor surface were measured simultaneously. Figure 3a shows the results obtained for the 5th overtone as a function of time for the following steps: flowing of rMrCP20, rinsing, flowing of $FeCl_3$ solution and second rinsing (see Materials and Methods). To allow direct comparison of the Δf and ΔD shifts measured at different harmonics, the net shifts of the 5th and 11th overtones are displayed in Fig. 3b, c. Upon injection of rMrCP20, an exponential increase in Δf intensity was measured (Fig. 3a), followed by a plateau, indicative of a rapid initial adsorption of rMrCP20 onto the Fe sensor surface followed by saturation at the surface. Δf recorded was $ca.$ −40.0 Hz and −39.2 Hz upon adsorption saturation for the 5th and 11th overtones, respectively. The significant decrease in Δf was accompanied by a proportional
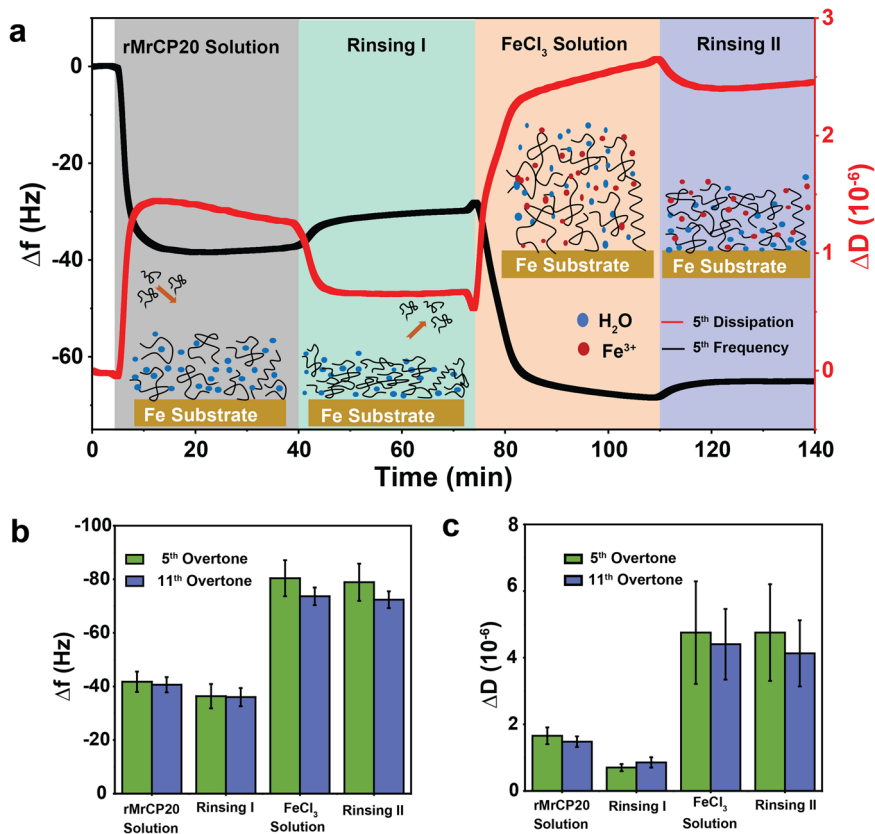
Fig. 3 QCM-D measurements tracking real-time adsorption of rMrCP20. a QCM-D frequency (Δf) shifts (left axis) and dissipation (ΔD) shifts (right axis) for 5th overtone as a function of time. The inset displays an illustration of protein structural changes upon adsorption and interaction with Fe^{3+}. Changes in frequency (**b**) and dissipation (**c**) obtained from the 5th and 11th overtones at different steps in QCM-D measurements. Error bars in the figure represent the SE from triplicate tests.

increase in ΔD to 1.62×10^{-6} and 1.55×10^{-6} for 5th and 11th overtones, respectively. Fast initial adsorption rates suggests that rMrCP20 has a high affinity for the Fe sensor surface, which can be driven by complementary electrostatic and hydrophobic adsorption[39–41]. The changes in Δf and ΔD due to rMrCP20 binding to the Fe sensor surface were generally similar amongst different overtones, indicating that the protein formed a compact and rigid layer[39]. While the inversely proportionate changes in ΔD and Δf denote the strong binding kinetics of rMrCP20 on Fe substrate, ΔD decreased gradually while Δf plateaued, suggesting that the adsorbed protein layer packed more tightly over time. The change of Δf was similar at different rMrCP20 concentrations, indicating that rMrCP20 formed a mono-adlayer (Supplementary Fig. 4c). Upon rinsing, a slight decrease in Δf intensity was detected due to the removal of excess unbound proteins, but most proteins remained strongly bound to the Fe surface.

The introduction of $FeCl_3$ induced large shifts in the QCM-D signals, splitting the response across the different harmonics (Supplementary Fig. 4a, b). The increase in Δf intensity indicates significant binding interaction between the analyte and adsorbed protein layer, which can occur via formation of Fe^{3+} metal-protein complexes and electrostatic interactions. The proportional increase in ΔD implies a more loose packing of the adlayer, which allows more ingression of water molecules that remained trapped within the adlayer[40]. Upon the final rinsing step to remove any loosely bound material, only a slight decrease in Δf intensity was observed, suggesting that Fe^{3+} ions were strongly bound to the pre-adsorbed rMrCP20 layer, whereas the slight decrease in ΔD indicates stiffening of the surface layer.

The mode of interaction between rMrCP20 and the metal surface can be deduced from the adsorption isotherms, which were obtained based on the results from weight loss measurements (Supplementary Table 1) to determine the adsorption characteristics of rMrCP20 on AH36 steel in buffer solution. The degree of surface coverage (θ) as a function of concentration (C) of the protein was fitted into various adsorption isotherm models, including Langmuir, Temkin, Freundlich, Flory–Huggins, Frumkin and El-Awady to identify the best fit based on the obtained R^2 values. The best fit was obtained for the Freundlich model ($R^2 = 0.96$, Supplementary Table 2), which is generally applicable for multilayer adsorption events on heterogeneous surfaces, with the assumption of a large number of different types of binding sites acting simultaneously[42–44]. The linear form of the Freundlich model can be written as[42]:

$$\log \theta = \frac{1}{n} \log C_{inh} + \log K_{ads} \tag{7}$$

where K_{ads} represents the Freundlich adsorption capacity (L mg^{-1}) and n describes the heterogeneity of the system related to the adsorption intensity. A larger n value connotes a more heterogeneous system, and $n > 1$ suggests a favorable adsorption process[45]. Freundlich constants K_{ads} and n values were 1.33×10^{-2} L mg^{-1} and 2.18, respectively. The value of K_{ads} was then used to calculate the standard free energy of adsorption (ΔG_{ads}^0)[31]:

$$\Delta G_{ads}^0 = -RT \ln\left(1 \times 10^6 K_{ads}\right) \tag{8}$$

where R is the universal gas constant, T is the absolute temperature, and 10^6 is the concentration of water molecules
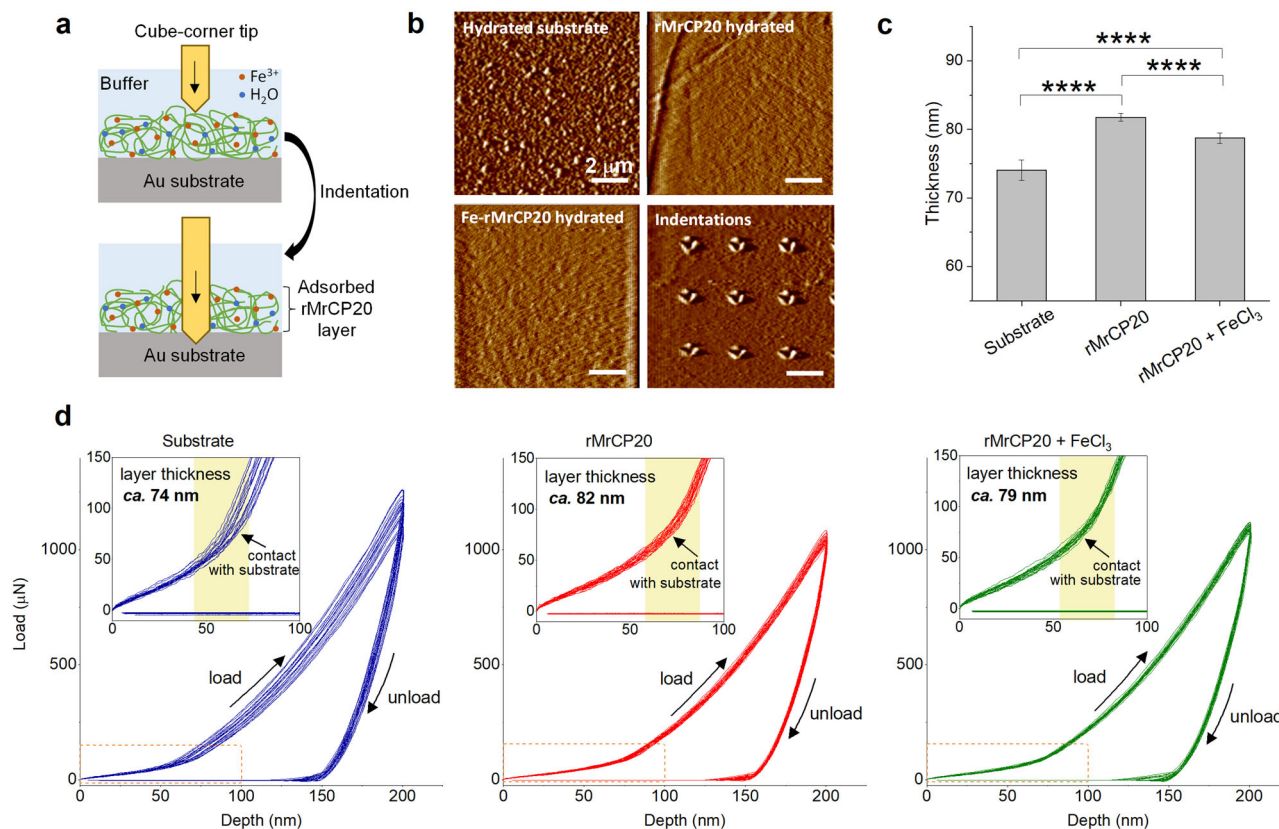
Fig. 4 Nanoindentation of *r*MrCP20 layer formed on substrate. a Illustration of indentation carried out with a cube-corner tip. **b** Scanning probe microscopy images of sample surfaces. **c** Bar plot of average values of layer thickness obtained by nanoindentation on substrate, substrate with adsorbed *r*MrCP20 layer, and substrate with *r*MrCP20 layer after interaction with FeCl$_3$. The average for each sample group is shown and SE indicated by error bars. All statistical significances difference between two groups are represented by *P*-value asterisk indicators with *P* < 0.0001 (****) and *P* < 0.001 (***). **d** Load-displacement (loading and unloading) curves with insets showing magnified views of the loading portion of indentation curves, where the change in slope was used to detect the substrate surface and infer the thickness of the protein film.

expressed in ppm. The calculated ΔG^0_{ads} value of $-23.52\ \text{kJ mol}^{-1}$ indicates spontaneous interaction between the protein and the surface of AH36 coupons, and is within the range for mixed adsorption involving both physisorption driven by electrostatic interactions as well as chemisorption caused by charge sharing or charge transfer from the protein molecules to the metal surface[33,46,47].

Since the QCM-D measurements have large dissipation values ($\Delta D > 0$), a viscoelastic model should be used to obtain more accurate adsorbed masses in QCM-D. However, analysis of soft and hydrated protein adlayers using the Voigt viscoelastic model has been shown to significantly deviate from values measured by surface plasmon resonance, a direct analysis to gain thickness from adlayer mass[48]. Therefore, to determine the thickness of *r*MrCP20 and its metal complex layer we carried out nanoindentation measurements (Fig. 4a) on *r*MrCP20 coated over a QCM-D sensor. Samples were equilibrated in buffer, and a cube-corner tip was used to indent the samples via a displacement-controlled indentation of 200 nm in depth. Figure 4b shows the surface roughness profile of the samples and Fig. 4c the histogram of the average layer thickness, indicating significant difference between samples. The layer thickness was inferred from the slope change during the loading step of indentation cycles, as illustrated in the load *vs.* displacement curves shown in Fig. 4d. The presence of a layer *ca.* 74 nm thick was consistently observed on the substrate when hydrated and was attributed to a thin oxide layer. Upon adsorption of *r*MrCP20, an indentation depth of *ca.* 82 nm was measured before the tip contacted the substrate,

indicating that the protein formed a layer of *ca.* 8 nm (subtracting the thickness of the oxide layer). Subsequent indentation of the protein layer after interaction with FeCl$_3$ showed a layer of thickness *ca.* 79 nm, indicating that the protein layer became slightly thinner (*ca.* 5 nm).

To assess the effect of Fe ions on *r*MrCP20 secondary structure and identify the type of binding interactions between Fe ions and the protein's side chains, ATR-FTIR spectroscopy measurements were conducted (Fig. 5). With *r*MrCP20 kept at 5 mg mL^{-1} concentration, different concentrations of FeCl$_3$ were added as indicated in Fig. 5a. The most significant changes in the spectra were observed at the protein:FeCl$_3$ molar concentration ratio of 1:60. At low FeCl$_3$ concentration, minimal changes were observed compared to *r*MrCP20-only spectra. The amide I band was further deconvoluted to obtain a semi-quantitative estimate of the secondary structural content, as shown in Fig. 5c. The initial β-sheet content of *r*MrCP20 protein was ~53% at 5 mg mL^{-1}. At the 1:60 protein:FeCl$_3$ concentration ratio, the amide I maximum of *r*MrCP20 spectra shifted from 1641 cm^{-1} to 1631 cm^{-1} (Fig. 5b), indicating a transition towards anti-parallel β-sheet structures. Similarly, the appearance of 1553 cm^{-1} in amide II confirm that FeCl$_3$ at high concentrations induced changes in the protein's conformation. The amide III peaks at 1262 cm^{-1} and 1296 cm^{-1} were likewise more noticeable at high FeCl$_3$ content.

New peaks were noticeable at higher concentrations of FeCl$_3$, indicating that new bonds formed between the protein and Fe^{3+}. The appearance of 800 cm^{-1} and 910 cm^{-1} bands were assigned to the stretching of aromatic –CH groups and C=C, respectively,
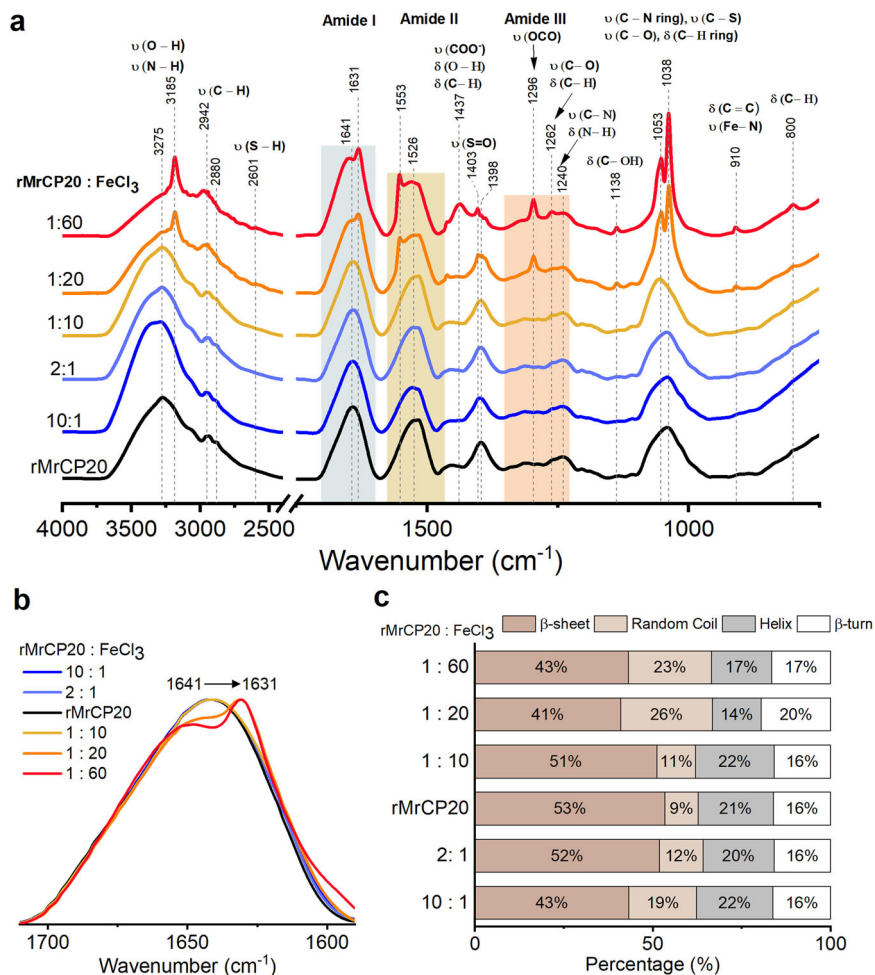
Fig. 5 FTIR-ATR investigation of the effect of FeCl$_3$ on rMrCP20 protein structure. a ATR-FTIR spectra of rMrCP20 and FeCl$_3$ at different molar concentration ratios, illustrating the spectral changes and bond assignments. **b** Shift in amide I band, indicating a transition of the protein secondary structure transiting towards anti-parallel β-sheets at higher FeCl$_3$ concentrations. **c** Semi-quantitative secondary structure based on amide I band deconvolution.

attributed to their interaction with Fe^{3+}. The distinct splitting of the band centered at 1043 cm^{-1} to 1038 cm^{-1} and 1053 cm^{-1} can be attributed to chelation of Fe^{3+} ions by the imidazole side chain of His[49]. The band at 1403 cm^{-1}, assigned as S = O bond appeared in the presence of Fe^{3+}, and was attributed to the oxidation of thiol functional groups of cysteine residues. The appearance of 1138 cm^{-1}, 1262 cm^{-1} and 1296 cm^{-1} bands were assigned to new interactions involving the protein's side chain C OH, C–O/–CH$_3$ and amide bond C = O functional groups, respectively. The intensity of the COO$^-$ stretching band of acidic residues at 1398 cm^{-1} observed for rMrCP20 decreased, concurrently with the appearance of a peak at 1437 cm^{-1} upon introduction of high FeCl$_3$ concentrations, is assigned to the formation of ionic bridges or coordination bonds between the carboxyl side chains and Fe^{3+} [49,50].

Small angle X-ray scattering and MD simulation studies of rMrCP20 and Fe ions. Small angle X-ray scattering (SAXS) was used to determine the radius of gyration (R_g) of rMrCP20 protein in our first steps towards developing a mechanistic model for the protein's adsorption to substrate surfaces (Supplementary Fig. 5a–c). The oligomeric state of rMrCP20 was obtained from SAXS experiments. SAXS profile of rMrCP20 were collected at 1.3, 4.1, and 6 mg mL^{-1}, respectively (Supplementary Fig. 5a). The scattering pattern of rMrCP20 at protein concentration of

1.3 mg mL^{-1} had a low signal to noise ratio and thus, no data pre-processing was performed with this dataset. R_g values using Guinier approximation of rMrCP20 at protein concentration of 4.1 and 6 mg mL^{-1} (Supplementary Table 3) showed a slight increase in molecular size, suggesting that the shift is most likely due to interparticle interaction between rMrCP20 molecules. To exclude the concentration-dependent effect, the results at protein concentration of 4.1 mg mL^{-1} were used for further data analysis. The overall structural parameters are recorded in Supplementary Table 3. Based on the Porod-volume (V_p) and DAMMIF-excluded volume (V_{ex}), determined from the scattering pattern at protein concentration of 4.1 mg mL^{-1}, the molecular weight (MW) of rMrCP20 was calculated to be 42 ± 4.2 and 45 ± 4.5 kDa, respectively (Supplementary Table 3). Knowing the calculated monomeric MW based on the protein sequences is 21 kDa, the data indicate that rMrCP20 adopts a dimeric state in solution at 4.1 mg mL^{-1}.

To investigate the distribution of Fe ions interacting with the protein and to calculate the number of Fe ions bound to each residue, MD simulations were performed for rMrCP20 protein dimer in the presence of a high Fe ion concentration. Two types of initial structures were considered. One is the NMR structure of rMrCP20 (PDB ID: 6LEK), another one is the structural model built by AlphaFold 2[51]. SAXS data showed rMrCP20 adopts a dimeric state in solution. Thus, the dimeric forms of both models
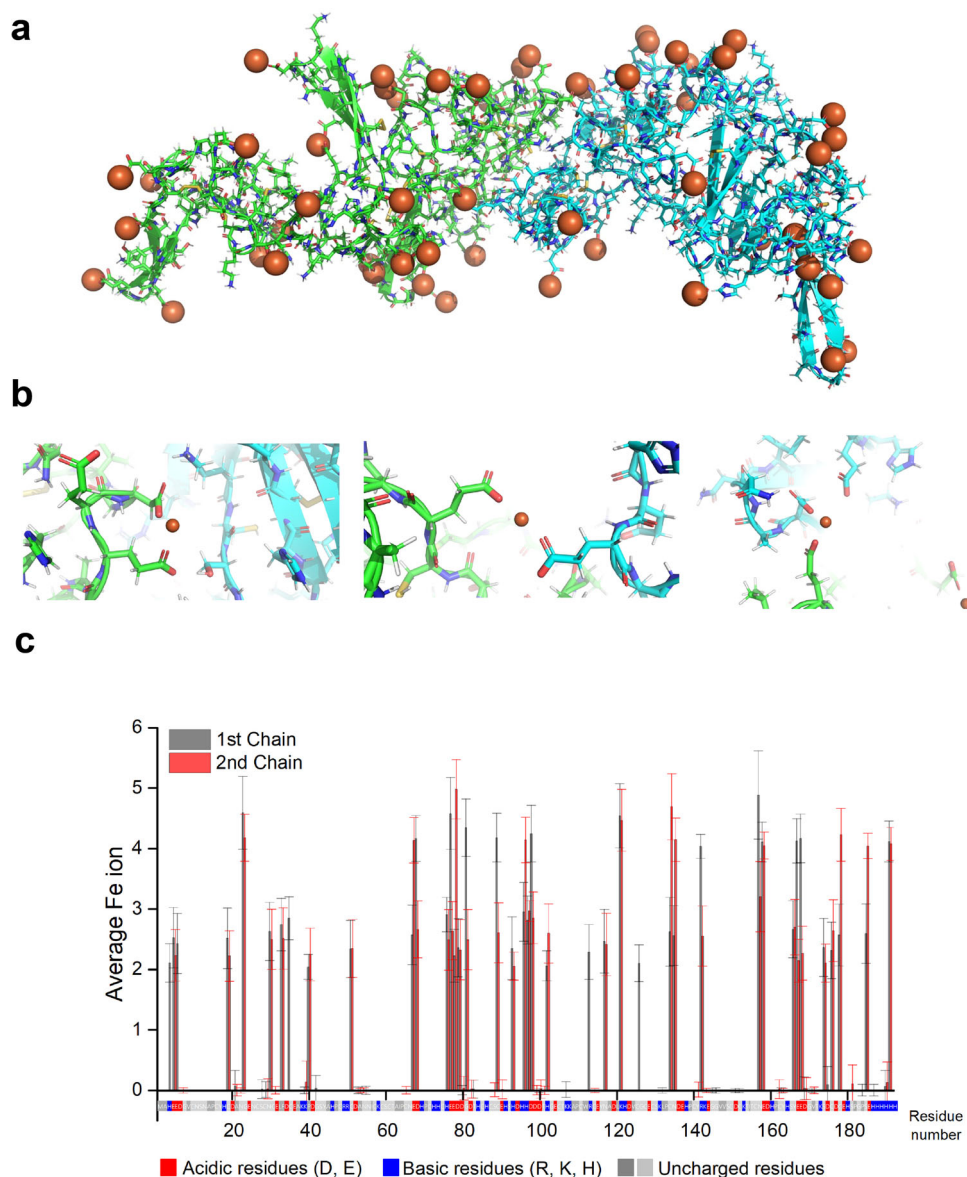
Fig. 6 MD simulation of *r*MrCP20 dimers in the presence of Fe ions. a Representative largest cluster structure of the protein dimer with each chain represented by a different color, illustrating the distribution of close-contacting Fe ions (orange spheres). **b**. Zoom-in view of Fe ions at the *r*MrCP20 interface. **c** Plot of average number of Fe ions bound to the residues, with color-coded protein sequence indicated below the plot. Error bars in the figure represent the SE.

were compared with the SAXS profile, and one of these dimers from AlphaFold 2 models showed a better fit, giving a χ^2 value of 1.76 (Supplementary Fig. 5d, e). This dimeric model was selected for subsequent MD simulation.

From the MD, the largest cluster structure with 54 close-contacting Fe ions around the protein dimer and the inset highlighting the interactions of Fe ions at *r*MrCP20 interface are shown in Fig. 6a, b. The average number of Fe ions bound to the residues is shown in Fig. 6c. The high root-mean-square-deviation (RMSD) obtained in MD simulation may reflect the intrinsic flexibility of the dimers in the presence of Fe ions (Supplementary Fig. 6), which predominantly interact with the negatively charged residues aspartic acid (Asp) and glutamic acid (Glu), binding up to more than 4 Fe ions, as shown in Fig. 6c. These Fe-protein interactions, especially those on the chain interfaces, may help to enhance protein-protein interactions, as experimentally observed from the spontaneous aggregation of *r*MrCP20 upon addition of FeCl$_3$ (see optical micrograph in

Supplementary Fig. 7). The results corroborate the FTIR data (Fig. 5a), notably the significant shift of the carboxyl band at high FeCl$_3$ concentration attributed to the interaction of Asp and Glu side chains with Fe ions, occurring in conjunction with changes in the protein's secondary structural conformation.

Proposed multimodal anti-corrosion mechanism. To further understand the adsorption behavior of *r*MrCP20, the AH36 substrate was incubated with fluorescein isothiocyanate (FITC)-labeled *r*MrCP20 and observed by fluorescence microscopy (Fig. 7a). Stronger fluorescence signals were observed at the GBs, indicating that more dye-protein conjugate accumulated at the GBs. Further investigations by AES and XPS were performed to confirm these observations. AH36 samples were incubated with *r*MrCP20 in 150 mM NaCl, pH 8.3 for 15 min, which were then rinsed with 150 mM NaCl solution and dried in air before analysis. Distinct AH36 grains and GBs were observed under SEM and the corresponding AES elemental mapping profiles (C, N, O)
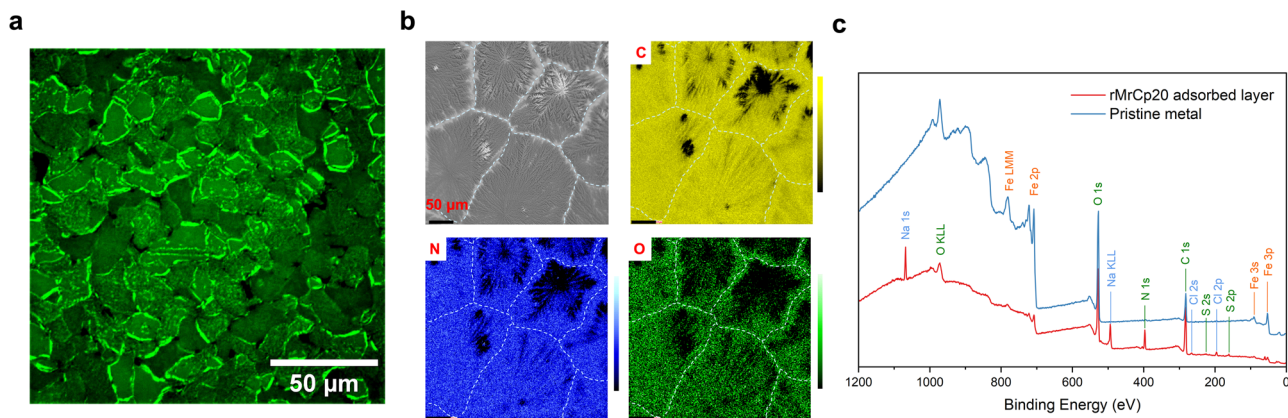
Fig. 7 Optical and electron microscope measurements of *r*MrCP20 layer formed on AH36 substrate. a Fluorescence image of FITC-labeled *r*MrCP20 layer on substrate. **b** SEM image and AES elemental mapping profiles (C, N, O) of adsorbed *r*MrCP20 layer. **c** The XPS survey spectra of *r*MrCP20 adsorbed layer and pristine metal. All scale bars are 50 μm.

with topographical corrections are shown in Fig. 7b. Surface topography corrections were carried out using the algorithm (P–B)/B[52], where B is the background signal and P is the Auger peak (Supplementary Fig. 8). We note that the signal intensities of the elements of interest were more pronounced at the GBs, indicating a higher concentration of *r*MrCP20 at these sites. GBs, which are inherently defective regions associated with grain misorientation, are usually less dense on atomic scale and tend to have higher free energies, thus potentially acting as preferential adsorption sites. We also conducted XPS mapping and verified the adsorption of the protein on a steel coupon (Fig. 7c), which can be inferred from the emergence of new peaks commonly associated with proteins. Further deconvolution of the high-resolution C 1s, N 1s, O 1s, and S 2p core-level spectra (Supplementary Fig. 9) revealed expected functional groups present for a protein, such as C=O amide bonds or C–S bonds associated with Cys residues, which are in close agreement with those obtained from the ATR-FTIR spectra (Fig. 5a). Overall, these data suggest preferential adsorption of *r*MrCP20 at the GBs, hence providing enhanced protection against aggressive corrosive ions.

Based on these findings, we propose a multimodal anti-corrosion activity by *r*MrCP20. *r*MrCP20 protein is highly negatively charged, comprising clusters of charged amino acids with a large number of 32 Cys residues that contribute to binding interactions with substrates, thereby allowing barnacles to adhere to charged surfaces such as metals[26,53]. The thiol side chain on Cys residues is easily deprotonated at seawater pH, leading to a negatively charged sulfhydryl group[54], which then binds to charged surface ions via electrostatic interactions[55] to form more stable thiolate-metal ion complexes[56]. The side chains of Asp and Glu residues are also deprotonated and negatively charged at seawater pH, hence favoring electrostatic interactions with cations. A multimodal corrosion inhibition mechanism is thereby illustrated in Fig. 8 to explain our findings. Corrosion of metal surfaces often occurs on or adjacent to GBs due to the different electrode potentials of the grain and boundary, making them susceptible to redox reactions that further lead to intergranular corrosion in the presence of electrolytes[57], while other forms of corrosions such as uniform, crevice and pitting corrosions also occur concurrently at the substrate-electrolyte interface[58,59]. *r*MrCP20 protein readily adsorbs onto metal substrate, preferentially filling GBs and coating the substrate surface thereby preventing direct contact between the substrate and seawater. The protein adheres strongly to the metal substrate through iron-protein interactions, hence blocking charge transfer path and functioning as a protective coating to inhibit different forms of corrosion.

Conclusion

*r*MrCP20 protein exhibits a concentration-dependent anti-corrosion property to effectively inhibit corrosion of AH36 steel substrates in solution at *r*MrCP20 concentrations above 5 mg mL^{-1}. The natural adhesive protein was shown to adsorb rapidly onto substrate surfaces, forming a relatively homogeneous layer that increases the impedance of the coating and reduces the propensity for spontaneous corrosion. The protein layer readily incorporates Fe ions, predominantly through electrostatic interactions with negatively charged residues at seawater pH conditions, concurrent with conformational changes in the protein's secondary structures, resulting in a thin proteinaceous film that enhances impermeability against seawater, thereby shielding the underlying substrate against aggressive corrosive ions. Our findings indicate that the barnacle adhesive protein *r*MrCP20 has promising potential for further scaling-up development into an effective and green anti-corrosion additive for steels in the marine environment. Alternatively, the study provides molecular-level guidelines to develop artificial protein-based corrosion inhibitors inspired by the primary and secondary structures of *r*MrCP20.

Materials and methods

rMrCP20 expression and purification. The detailed expression and purification protocol of *r*MrCP20 was described in Mohan-ram et al.[26]. Briefly, an ampicillin - resistant pET-22b(+) vector with cloned cDNA of CP20 (Uniprot Q9GRC4) and C terminal his-tag was purchased from Bio Basic (Singapore). The plasmid was then transformed into chemically competent *Escherichia coli* BL21 (DE3) cells. A single colony transformants of *r*MrCP20 were grown in Luria-Bertani medium with 100 μg mL^{-1} ampicillin at 37 °C and expressed using 1 mM IPTG (Isopropyl thio-β-D-galactoside) at 20 °C. The harvested cells were then lysed via probe sonication (40% amplitude, 1 s pulse + 1 s pause, 20 min) and the crude lysate after high-speed centrifugation was purified by affinity chromatography (Ni-NTA affinity column, GE Healthcare Life Sciences, HisTrap, 5 mL). The eluted protein was further purified using size-exclusion chromatography (SEC) (Superdex 75, 16/600) using isocratic elution in 20 mM Tris, 150 mM NaCl, at pH 8.3. The fractions containing *r*MrCP20 were concentrated to the required concentration using Vivaspin column (M.W. cutoff 5 kDa). The protein concentration measurements were done using absorbance spectrometry at 280 nm (Nanodrop 2000c).

Preparation of steel coupons. AH36 steel coupons cut to 10 × 10 × 2 mm were purchased from Ebenezer Excel
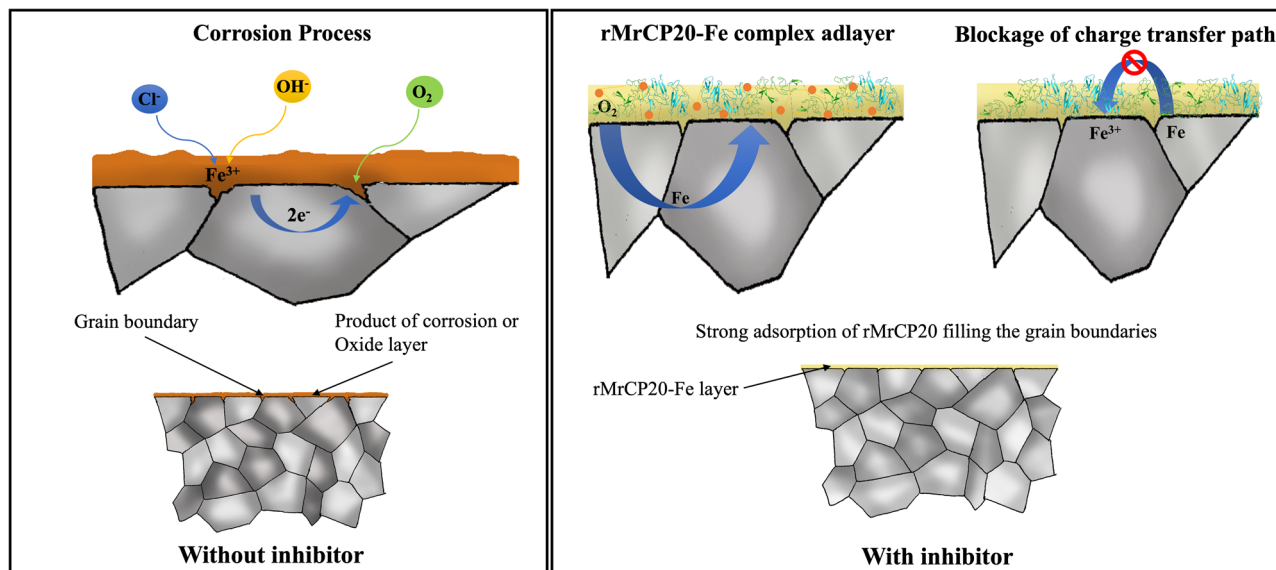
Fig. 8 Proposed multimodal corrosion inhibition action of *r*MrCP20 protein on steel substrates. The corrosion inhibition action of *r*MrCP20 is attributed to the adhesive property of the protein and its ability to spontaneously bind with free Fe ions.

Engineering, Singapore. Chemical composition (in wt %) of the AH36 material was Nb 0.03, Cr 0.03, Mn 0.2 and the balance Fe. The coupons were embedded in cold mount epoxy (EpoFix, Struers), while for electrochemical studies, coupons were welded with an electrical wire before embedding in epoxy. Prior to all experiments, grinding was performed manually with a series of grit paper (# 800 to # 2000) to expose a surface area of 1 cm^2 and then polished to a mirror-like finish using a diamond suspension (Ø = 3 μm, Struers) to alleviate the effects of surface roughness on protein absorption[60]. The samples were then washed with Milli-Q water (18.2 MΩ cm, Millipore^{TM}), cleaned with ethanol in an ultrasonic bath, washed again with Milli-Q water and finally dried with nitrogen gas[36].

Time-resolved corrosion study of on AH36 coupon. AH36 steel samples were immersed in a buffer solution with different *r*MrCP20 protein concentrations (0.1, 0.5, 1, 3, 5 and 10 mg mL^{-1}) and incubated at ambient temperature, on an orbital shaker set at 150 rpm for 24 h. AH36 steel samples were removed at stipulated time points for visual inspection, and subsequently removed after 24 h for collecting corrosion-products on the coupons and from buffer solution. Experiments were triplicated, using freshly prepared AH36 steel coupons.

Weight loss measurements. To quantify the total Fe mass loss after incubation, both Fe content from corrosion products bound to sample surfaces and Fe content dissolved in incubation solutions were collected and measured using inductively coupled plasma optical emission spectrophotometer (ICP-OES) (PerkinElmer® Optima™ 8300). Corrosion products bound to the sample surfaces were removed with 10 min of ultrasonication in 5 mL of 1% HCl solution containing 100 mM hexamethylenetetramine (Sigma-Aldrich) for preventing additional Fe dissolution from the coupons[27]. 1 mL of the respective Fe solutions were dissolved separately in 9 mL of 10% HNO$_3$, then further diluted by 10x in Milli-Q water and filtered through 0.45 μm membrane prior to ICP-OES measurements. Calibration for Fe concentration standard curve was first performed using 5, 10, 25, 50 and 100 ppm standard solutions, and the wavelength for metal detection was Fe 238.86 nm. All experiments were performed in triplicates.

Electrochemical measurements. Electrochemical measurements including electrochemical impedance spectroscopy (EIS) and potentiodynamic polarization (PDP) were conducted using PGSTAT302N Autolab (Metrohm) with NOVA 2.1 software. The conventional three-electrode system was used, in which the reference and working electrodes were saturated Ag/AgCl and AH36 steel with a single side of 10 × 10 mm exposed square area, respectively. A platinum sheet of 20 × 10 mm was chosen as the counter electrode as the area needs to be larger than the exposed working electrode to guarantee uniformity of the electrochemical reaction[61]. The working electrode was exposed to buffer solution containing various *r*MrCP20 concentrations. All electrochemical measurements were performed at room temperature and repeated in triplicate.

Prior to measurements, the working electrode was incubated in a test solution for 30 min under stagnant condition until a stable open circuit potential (OCP) was attained. EIS measurements at different time intervals were conducted with a perturbation amplitude of 10 mV at OCP over a frequency range of 0.01–10000 Hz. The NOVA 2.1 software was employed for analysis of the EIS spectra. Nyquist and Bode plots were drawn by fitting the impedance data using equivalent circuit.

Potentiodynamic polarization (PDP) experiments were carried out after 24 h of exposure, in the potential range from −0.25 V versus OCP to −0.4 V versus Ag/AgCl with the sweep rate of 10 mV min^{-1}. The corrosion potential (E$_{corr}$) and corrosion current density (i$_{corr}$) were calculated by extrapolating the linear Tafel segments of the anodic and cathodic curves. The data processing was performed using the NOVA 2.1 software.

Quartz Crystal Microbalance with dissipation monitoring, QCM-D. The adsorption of *r*MrCP20 on Fe substrate and its interaction with Fe^{3+} were analyzed using Quartz Crystal Microbalance (QCM) with Dissipation monitoring (Q-Sense E4 QCM, Sweden), connected with IPC peristatic pump (Ismatec SA, Switzerland). The iron-coated quartz crystals with a fundamental frequency of 4.95 MHz were purchased from Q-sense (QSX 319, Biolin Scientific). All QCM sensor crystals were cleaned according to a standard protocol whereby the surface is immersed in 1% Hellmanex III (Sigma-Aldrich) solution for 30 min, then ultrasonicated in 99% ethanol (Merck) for 10 min, followed by rinsing

with Milli-Q water and finally dried with nitrogen gas. These measurements were carried out at a constant flow rate of 100 μL min^{-1} and the temperature of the measuring cell was controlled at 22 °C. The resonant frequency of the oscillator (f) and the energy dissipation value (D) were recorded simultaneously as a function of time. The system baseline was established for 1 h using the buffer solution without protein. After stabilization, 23 μM of rMrCP20 solution was injected and the adsorption took place for 45 min. The cell was then rinsed with buffer until stable frequency and dissipation values were attained. 100 μM of FeCl$_3$ solution was injected and the adsorption of FeCl$_3$ on pre-adsorbed protein layer took place for 35 min. Buffer was then re-introduced to wash out the weak bound complexes.

Attenuated total reflectance Fourier-transform infrared spectroscopy (ATR-FTIR). Samples were prepared at 1 and 5 mg mL^{-1} rMrCP20 protein concentration with a series of FeCl$_3$ concentrations in separate vials of 100 μL volume and incubated at ambient temperature for 1 h, by dipping the vials in liquid N$_2$ for 5 min and lyophilized immediately. Attenuated total reflection fourier-transform infrared (ATR-FTIR) spectroscopy measurements were performed on a Bruker Vertex 70 (Massachusetts, USA) instrument equipped with a PIKE Technologies MIRacle attenuated total reflection (ATR) Diamond-ZnSe 3-reflection accessory and a LN$_2$ cooled MCT detector. Scans were obtained at ambient temperature over the range of 4000 to 750 cm^{-1} with a resolution of 2 cm^{-1}, averaged over scans obtained at 20 kHz for 1 min. All spectra processing were performed on OPUS 6.5, in the sequence of water vapor subtraction, background subtraction of buffer, baseline correction, and min-max normalization using amide I band. Amide I band was deconvoluted by secondary derivation, with peak fitting performed using 100% Gaussian curves with individual FWHM kept relatively consistent. The deconvoluted peaks were then assigned to the respective secondary structures[40,51–53].

Nanoindentation. QCM sensors (same as above) were first cleaned with ethanol and Milli-Q water, then dried with nitrogen gas. Each sensor was then incubated separately in 5 mL of 5 mg mL^{-1} rMrCP20 protein solution for 50 min in 12-well plates, followed by 5 mL of buffer for 50 min. Half of the sensors were then incubated in 4 mL of 50 μM FeCl$_3$ for 40 min, followed by 4 mL of buffer for 40 min. All incubations were performed on a shaker. Nanoindentation was performed with a Hysitron TI 950 Triboindenter (Minnesota, USA), using a Berkovich (cube-corner) indentation tip. The tip was calibrated with a fused quartz standard sample of $\overline{E} = 69.9$ GPa ± 10%. Sensors were attached to magnetic stainless steel specimen discs and placed on a standard stage, then tip to optic calibrations were performed prior to lifting the tip 100 μm above sample and adding a drop of water on the sample, allowing the tip to submerge and equilibrate. After 30 min, indentations were performed with displacement-controlled setting of 200 nm depth. Load–hold–unload indentation function setup was applied for all indents, with segment intervals of 5 s (load), 2 s (hold), and 5 s (unload). At least 30 indents were obtained for each sample. Slope tangents were obtained separately from contact with sample layer and substrate, and intersections of the tangents indicated the sample layer thickness. Statistical significance between groups were acquired via two-sample t-test assuming unequal variances. P-value of $P < 0.0001$ (****) and $P < 0.001$ (***) represented significance difference between two groups.

Field emission scanning electron microscopy – energy dispersive X-ray (FESEM-EDX). AH36 coupons were adhered to sample stubs with adhesive carbon tape, and copper tape. Without coating, imaging was performed using JEOL JSM-FESEM 7800F PRIME (Massachusetts, USA), at SEI-mode, 20 kV, and 92 μA emission current. EDX maps were acquired at a 20 keV, 1024 resolution, with fixed duration of 3 frame counts, and process time 4, and pixel dwell time of 20 μs.

SAXS data collection and analysis. SAXS data for rMrCP20 were collected with a Xenocs Nano-inXider SAXS instrument equipped with a microfocus sealed-tube X-ray source (Cu, 30 W, 40 μm focus) and a Dectris Pilatus 3hybrid pixel detector. The X-rays are filtered through the two-dimensional single-reflection multilayer optics and collimated by a three-pinhole system. The sample-to-detector distance was set at 0.94 m, and the sample chamber and X-ray paths were evacuated prior to usage. This setup covers a range of momentum transfer of $0.08 < q < 4$ nm^{-1} [$q = 4\pi\sin(\theta)/\lambda$, where 2θ is the scattering angle]. SAXS experiments of rMrCP20 were carried out at room temperature in the buffer composed of 20 mM Tris-HCl, pH 8.3 and 150 mM NaCl, using the low-noise flow cell. The protein concentrations used were 1.3, 4.1 and 6 mg mL^{-1}. The data were collected for 45 min, and for each measurement a total of nine frames at 5 min intervals were recorded. The scattered X-rays detected by a two-dimensional area detector were converted to one-dimensional scattering using the built-in SAXS software (Xenocs).

All the data processing steps were performed using the program package PRIMUS[62,63]. The scattering of the buffer was subtracted from the data. The experimental data obtained were analyzed for aggregation using a Guinier plot[64]. The forward scattering, $I(0)$ and the radius of gyration, R_g, were computed using the Guinier approximation, which assumes that at very small angles ($q < 1.3/R_g$), the intensity is represented as $I(q) = I(0) \times \exp[-(qR_g)^{\frac{2}{3}}]$[64]. These parameters were also computed from the extended scattering patterns using the indirect transform package GNOM[65], which provides the distance distribution function, $P(r)$, and hence the maximal particle dimension, D_{max}, and the radius of gyration, R_g. The hydrated volume, V_p, which was used to estimate the molecular mass of the protein, was computed using the Porod invariant. The theoretical scattering profiles were generated from the atomic resolution structure of rMrCP20 (PDB ID: 6LEK state 1) by considering both monomeric and dimeric structures, and the simulated models generated in this study. All generated theoretical scattering profiles were evaluated against the experimental scattering profile using CRYSOL[66].

Molecular dynamics simulations. *Initial Structure*. AlphaFold2 server[67] was used to predict the structure of rMrCP20 in monomeric and dimeric forms. One of the dimeric form was found to be better consistent with the SAXS data in that the theoretical scattering profile of the dimeric structure calculated using CRYSOL[63] fitted well with the experimental profile ($\chi^2 = 1.76$). Thus, this dimeric structure was taken as the initial structure for the following molecular dynamics simulation.

The rMrCP20 dimer was represented by AMBER99SB-ILDN force field[68]. The system were solvated with 161,769 TIP3P[69] water molecules, 802 Fe^{3+} ions and 2354 chloride ions were added to neutralize the system. The system was put in a cubic box of 173 Angstroms with periodic boundary condition. The molecular dynamics (MD) simulation used GROMACS[70] 5.1.2 software. The LINCS[71] algorithm was used to constrain bonds between heavy atoms and hydrogen to enable a timestep of 2 fs. A 1.2 nm cutoff was used for Van der Waals interaction and short-range electrostatic interactions calculations, and Particle Mesh Ewald method was implemented for long range electrostatic

calculations. Simulation temperature was maintained at 300 K using a V-rescale thermostat[72] and 1 bar pressure using Parrinello-Rahman[73] barostat. A production run of 100 ns was obtained.

Fluorescence microscopy. *r*MrCP20 was labeled with FITC (fluorescein isothiocyanate, Sigma-Aldrich) using the same protocol as previously described[74]. Briefly, 3 mg mL^{-1} of FTIC was dissolved in acetone and 200 μL was slowly added to 4 mL of *r*MrCP20 at 7 mg mL^{-1} in 150 mM NaCl, 20 mM Tris, pH 8.3 buffer. The reaction mixture was incubated overnight at 4 °C. The FITC-*r*MrCP20 mixture was then subjected to a PD-10 gel filtration column (GE healthcare life sciences) and eluted with buffer solution (150 mM NaCl, 20 mM Tris, pH 8.3). To view the GB under microscopy, AH36 substrate was polished to mirror surface quality and slightly etched with 2% Nital solution. The FITC-*r*MrCP20 solution was then cast on an AH36 etched substrate and rinsed with buffer to remove the loosely bound proteins. The images were obtained with an inverted microscope (Zeiss Axio Observer, Z2).

Auger electron spectroscopy (AES) data were obtained using a field-emission Auger microprobe (JEOL JAMP-7830F) with a primary electron beam having an accelerating voltage of 10 keV and a probe current of 10 nA. The sample was tilted at 30° throughout the analysis. AES elemental mapping was collected with a pixel density of 256 × 256 and a dwell time of 10 ms. The mapping was acquired by setting the analyzer to a specific Auger peak (P) energy and background (B) energy, operated at a constant retarding ratio of 0.6 for high sensitivity analysis. To correct for the topographical effects, the data were processed using the (P − B)/B algorithm.

X-ray photoelectron spectroscopy (XPS) analysis was performed using an AXIS Supra spectrometer (Kratos Analytical, UK) equipped with a hemispherical analyzer and a monochromatic Al K-alpha source (1487 eV) operated at 15 mA and 15 kV. The XPS spectra were acquired from an area of 700 × 300 μm^2 with a take-off angle of 90°. Pass energy of 160 eV and 20 eV were used for survey and high-resolution scans, respectively. A 3.1-volt bias was applied to the sample to neutralize charge build up on the sample surface. The binding energies (BEs) were charge-corrected based on the C 1s of adventitious carbon at 284.8 eV. The data processing was performed using the ESCApe software.

Data availability

All data are available in the main text and supplementary materials. Any additional data are available from the corresponding author upon request.

References

1. Jeong, H. H. et al. Corrosion-Protected Hybrid Nanoparticles. *Adv. Sci.* **4**, 1700234 (2017).
2. Olajire, A. A. Corrosion inhibition of offshore oil and gas production facilities using organic compound inhibitors-A review. *J. Mol. Liquids* **248**, 775–808 (2017).
3. Kirchgeorg, T. et al. Emissions from corrosion protection systems of offshore wind farms: Evaluation of the potential impact on the marine environment. *Marine Poll. Bull.* **136**, 257–268 (2018).
4. McMahon, M. E. et al. A review of modern assessment methods for metal and metal-oxide based primers for substrate corrosion protection. *Front. Mater.* **6**, 190 (2019).
5. Dutta, A., Saha, S. K., Banerjee, P. & Sukul, D. Correlating electronic structure with corrosion inhibition potentiality of some bis-benzimidazole derivatives for mild steel in hydrochloric acid: combined experimental and theoretical studies. *Corros. Sci.* **98**, 541–550 (2015).
6. Saji, V. S., A review on recent patents in corrosion inhibitors. *Recent Patents Corros. Sci.*, **2**, 6–12 (2010).
7. Bedir, A. G., Abd El-raouf, M., Abdel-Mawgoud, S., Negm, N. A. & El Basiony, N. Corrosion Inhibition of Carbon Steel in Hydrochloric Acid Solution Using Ethoxylated Nonionic Surfactants Based on Schiff Base: Electrochemical and Computational Investigations. *ACS Omega* **6**, 4300–4312 (2021).
8. Naderi, E., Jafari, A., Ehteshamzadeh, M. & Hosseini, M. Effect of carbon steel microstructures and molecular structure of two new Schiff base compounds on inhibition performance in 1 M HCl solution by EIS. *Mater. Chem. Phys.* **115**, 852–858 (2009).
9. Lece, H. D., Emregül, K. C. & Atakol, O. Difference in the inhibitive effect of some Schiff base compounds containing oxygen, nitrogen and sulfur donors. *Corros. Sci.* **50**, 1460–1468 (2008).
10. Dehdab, M., Shahraki, M. & Habibi-Khorassani, S. M. Theoretical study of inhibition efficiencies of some amino acids on corrosion of carbon steel in acidic media: green corrosion inhibitors. *Amino Acids* **48**, 291–306 (2016).
11. Khaled, K. & Abdel-Shafi, N. Quantitative structure and activity relationship modeling study of corrosion inhibitors: Genetic function approximation and molecular dynamics simulation methods. *Int. J. Electrochem. Sci.* **6**, 4077–4094 (2011).
12. Hosseini, S. & Azimi, A. The inhibition of mild steel corrosion in acidic medium by 1-methyl-3-pyridin-2-yl-thiourea. *Corros. Sci.* **51**, 728–732 (2009).
13. Caliskan, N. & Akbas, E. Corrosion inhibition of austenitic stainless steel by some pyrimidine compounds in hydrochloric acid. *Mater. Corros.* **63**, 231–237 (2012).
14. Abd El-Lateef, H. M. Experimental and computational investigation on the corrosion inhibition characteristics of mild steel by some novel synthesized imines in hydrochloric acid solutions. *Corros. Sci.* **92**, 104–117 (2015).
15. Marzorati, S., Verotta, L. & Trasatti, S. P. Green corrosion inhibitors from natural sources and biomass wastes. *Molecules* **24**, 48 (2018).
16. Amin, M. A., Khaled, K., Mohsen, Q. & Arida, H. A study of the inhibition of iron corrosion in HCl solutions by some amino acids. *Corros. Sci.* **52**, 1684–1695 (2010).
17. Hamadi, L., Mansouri, S., Oulmi, K. & Kareche, A. The use of amino acids as corrosion inhibitors for metals: A review. *Egypt. J. Petroleum* **27**, 1157–1165 (2018).
18. Barouni, K. et al. Some amino acids as corrosion inhibitors for copper in nitric acid solution. *Mater. Lett.* **62**, 3325–3327 (2008).
19. Zhang, F. et al. Investigation and application of mussel adhesive protein nanocomposite film-forming inhibitor for reinforced concrete engineering. *Corros. Sci.* **153**, 333–340 (2019).
20. Hou, R.-Q. et al. Corrosion inhibition of pre-formed mussel adhesive protein (Mefp-1) film to magnesium alloy. *Corros. Sci.* **164**, 108309 (2020).
21. Zhang, F. & Pan, J. Recent development of corrosion protection strategy based on mussel adhesive protein. *Front. Mater.* **6**, 207 (2019).
22. Zhang, F., Pan, J., Claesson, P. M. & Brinck, T. Electrochemical, atomic force microscopy and infrared reflection absorption spectroscopy studies of pre-formed mussel adhesive protein films on carbon steel for corrosion protection. *Thin Solid Films* **520**, 7136–7143 (2012).
23. Blackwood, D. J., Lim, C. S., Teo, S. L., Hu, X. & Pang, J. Macrofouling induced localized corrosion of stainless steel in Singapore seawater. *Corros. Sci.* **129**, 152–160 (2017).
24. Eashwar, M., Subramanian, G., Chandrasekaran, P. & Balakrishnan, K. Mechanism for barnacle-induced crevice corrosion in stainless steel. *Corrosion* **48**, 608–612 (1992).
25. Wiegemann, M. & Watermann, B. Peculiarities of barnacle adhesive cured on non-stick surfaces. *J. Adhes. Sci. Technol.* **17**, 1957–1977 (2003).
26. Mohanram, H., Kumar, A., Verma, C. S., Pervushin, K. & Miserez, A. Three-dimensional structure of Megabalanus rosa Cement Protein 20 revealed by multi-dimensional NMR and molecular dynamics simulations. *Philos. Trans. R. Soc. B* **374**, 20190198 (2019).
27. Murugan, V. K. et al. Accelerated corrosion of marine-grade steel by a redox-active, cysteine-rich barnacle cement protein. *npj Mater. Degrad.* **4**, 1–8 (2020).
28. Fouda, A. E.-A. S. et al. Experimental and computational chemical studies on the corrosion inhibitive properties of carbonitrile compounds for carbon steel in aqueous solutions. *Sci. Rep.* **11**, 1–24 (2021).
29. Lou, Y. et al. Microbiologically influenced corrosion inhibition of carbon steel via biomineralization induced by Shewanella putrefaciens. *npj Mater. Degrad.* **5**, 1–11 (2021).
30. Umoren, S., Solomon, M. M., Israel, A. U., Eduok, U. M. & Jonah, A. E. Comparative study of the corrosion inhibition efficacy of polypropylene glycol and poly (methacrylic acid) for mild steel in acid solution. *J. Dispersion Sci. Technol.* **36**, 1721–1735 (2015).

31. Solomon, M. M., Gerengi, H. & Umoren, S. A. Carboxymethyl cellulose/silver nanoparticles composite: synthesis, characterization and application as a benign corrosion inhibitor for St37 steel in 15% H2SO4 medium. *ACS Appl. Materm Interfaces* **9**, 6376–6389 (2017).

32. Bai, L. et al. Comparison of the synergistic effect of counterions on the inhibition of mild steel corrosion in acid solution: electrochemical, gravimetric and thermodynamic studies. *RSC Adv.* **5**, 4716–4726 (2015).

33. Solomon, M. M., Umoren, S. A., Obot, I. B., Sorour, A. A. & Gerengi, H. Exploration of dextran for application as corrosion inhibitor for steel in strong acid environment: effect of molecular weight, modification, and temperature on efficiency. *ACS Appl. Mater. Interfaces* **10**, 28112–28129 (2018).

34. Zheng, X., Zhang, S., Gong, M. & Li, W. Experimental and theoretical study on the corrosion inhibition of mild steel by 1-octyl-3-methylimidazolium L-prolinate in sulfuric acid solution. *Ind. Eng. Chem. Res.* **53**, 16349–16358 (2014).

35. Hari Kumar, S. & Karthikeyan, S. Torsemide and furosemide as green inhibitors for the corrosion of mild steel in hydrochloric acid medium. *Ind. Eng. Chem. Res.* **52**, 7457–7469 (2013).

36. Zhang, F., Pan, J. & Claesson, P. M. Electrochemical and AFM studies of mussel adhesive protein (Mefp-1) as corrosion inhibitor for carbon steel. *Electrochim. Acta* **56**, 1636–1645 (2011).

37. Farhadian, A. et al. Exploration of sunflower oil as a renewable biomass source to develop scalable and highly effective corrosion inhibitors in a 15% HCl medium at high temperatures. *ACS Appl. Mater. Interfaces* **13**, 3119–3138 (2021).

38. Solomon, M. M. & Umoren, S. A. In-situ preparation, characterization and anticorrosion property of polypropylene glycol/silver nanoparticles composite for mild steel corrosion in acid solution. *J. Colloid Interface Sci.* **462**, 29–41 (2016).

39. Biggs, S., Labarre, M., Hodges, C., Walker, L. M. & Webber, G. B. Polymerized rodlike micelle adsorption at the solid− liquid interface. *Langmuir* **23**, 8094–8102 (2007).

40. Zhang, F. et al. In situ investigations of Fe3+ induced complexation of adsorbed Mefp-1 protein film on iron substrate. *J. Colloid Interface Sci.* **404**, 62–71 (2013).

41. Sebastiani, F., Arteta, M. Y., Lindfors, L. & Cárdenas, M. Screening of the binding affinity of serum proteins to lipid nanoparticles in a cell free environment. *J. Colloid Interface Sci.* **610**, 766–774 (2022).

42. Deyab, M., Essehli, R. & El Bali, B. Inhibition of copper corrosion in cooling seawater under flowing conditions by novel pyrophosphate. *RSC Adv.* **5**, 64326–64334 (2015).

43. Umpleby, R. J. II et al. Application of the Freundlich adsorption isotherm in the characterization of molecularly imprinted polymers. *Anal. Chim. Acta* **435**, 35–42 (2001).

44. Skopp, J. Derivation of the Freundlich adsorption isotherm from kinetics. *J. Chem. Educ.* **86**, 1341 (2009).

45. Pandian, A., Karthikeyan, C. & Rajasimman, M. Isotherm and kinetic studies on adsorption of malachite green using chemically synthesized silver nanoparticles. *Nanotechnol. Environ. Eng.* **2**, 1–17 (2017).

46. Yüce, A. O., Mert, B. D., Kardaş, G. & Yazıcı, B. Electrochemical and quantum chemical studies of 2-amino-4-methyl-thiazole as corrosion inhibitor for mild steel in HCl solution. *Corros. Sci.* **83**, 310–316 (2014).

47. Pavithra, M., Venkatesha, T., Kumar, M. P. & Tondan, H. Inhibition of mild steel corrosion by Rabeprazole sulfide. *Corros. Sci.* **60**, 104–111 (2012).

48. Spirk, S., Palasingh, C. & Nypelö, T. Current opportunities and challenges in biopolymer thin film analysis—Determination of film thickness. *Front. Chem. Eng.* **3**, 755446 (2021).

49. Schwaminger, S. P. et al. Nature of interactions of amino acids with bare magnetite nanoparticles. *J. Phys. Chem. C* **119**, 23032–23041 (2015).

50. Alhazmi, H. A. FT-IR spectroscopy for the identification of binding sites and measurements of the binding interactions of important metal ions with bovine serum albumin. *Sci. Pharm.* **87**, 5 (2019).

51. Jumper, J. et al. Highly accurate protein structure prediction with AlphaFold. *Nature* **596**, 583–589 (2021).

52. Watts, J. F., Wolstenholme, J., *An introduction to surface analysis by XPS and AES* (John Wiley & Sons, 2019).

53. KAMINO, K. Novel barnacle underwater adhesive protein is a charged amino acid-rich protein constituted by a Cys-rich repetitive sequence. *Biochem. J.* **356**, 503–507 (2001).

54. Kumar, A. et al. Disorder–Order Interplay of a Barnacle Cement Protein Triggered by Interactions with Calcium and Carbonate Ions: A Molecular Dynamics Study. *Chem. Mater.* **32**, 8845–8859 (2020).

55. Lai, W.-L. et al. The functional role of the binuclear metal center in D-aminoacylase: one-metal activation and second-metal attenuation. *J. Biol. Chem.* **279**, 13962–13967 (2004).

56. Wang, S. et al. Single molecule observation of hard–soft-acid–base (HSAB) interaction in engineered Mycobacterium smegmatis porin A (MspA) nanopores. *Chem. Sci.* **11**, 879–887 (2020).

57. Barr, C. M. et al. Tracking the evolution of intergranular corrosion through twin-related domains in grain boundary networks. *npj Mater. Degrad.* **2**, 1–10 (2018).

58. Jones, K. & Hoeppner, D. W. The interaction between pitting corrosion, grain boundaries, and constituent particles during corrosion fatigue of 7075-T6 aluminum alloy. *Int. J. Fatigue* **31**, 686–692 (2009).

59. Guo, X. et al. Near-field corrosion interactions between glass and corrosion resistant alloys. *npj Mater. Degrad.* **4**, 1–15 (2020).

60. Rechendorff, K., Hovgaard, M. B., Foss, M., Zhdanov, V. & Besenbacher, F. Enhancement of protein adsorption induced by surface roughness. *Langmuir* **22**, 10885–10888 (2006).

61. Shi, X., Xiu, S. & Liu, X. Experiment study on the corrosion resistance of the surface metamorphic layer of grinding. *Sci. Rep.* **11**, 1–12 (2021).

62. Konarev, P. V., Volkov, V. V., Petoukhov, M. V. & Svergun, D. I. ATSAS 2.1, a program package for small-angle scattering data analysis. *J. Appl. Crystallogr.* **39**, 277–286 (2006).

63. Konarev, P. V., Volkov, V. V., Sokolova, A. V., Koch, M. H. J. & Svergun, D. I. PRIMUS: a Windows PC-based system for small-angle scattering data analysis. *J. Appl. Crystallogr.* **36**, 1277–1282 (2003).

64. Guinier, A. La diffraction des rayons X aux très petits angles: application à l'étude de phénomènes ultramicroscopiques. *Ann. De Phys.* **11**, 161–237 (1939).

65. Svergun, D. I. Determination of the regularization parameter in indirect-transform methods using perceptual criteria. *J. Appl. Crystallogr.* **25**, 495–503 (1992).

66. Svergun, D., Barberato, C. & Koch, M. H. J. CRYSOL– a Program to Evaluate X-ray Solution Scattering of Biological Macromolecules from Atomic Coordinates. *J. Appl. Crystallogr.* **28**, 768–773 (1995).

67. Mirdita, M. et al. ColabFold: making protein folding accessible to all. *Nat. Methods*, **19**, 679–682 (2022).

68. Lindorff-Larsen, K. et al. Improved side-chain torsion potentials for the Amber ff99SB protein force field. *Proteins* **78**, 1950–1958 (2010).

69. Jorgensen, W. L., Chandrasekhar, J., Madura, J. D., Impey, R. W. & Klein, M. L. Comparison of simple potential functions for simulating liquid water. *J. Chem. Phys.* **79**, 926–935 (1983).

70. Van Der Spoel, D. et al. GROMACS: fast, flexible, and free. *J. Comput. Chem.* **26**, 1701–1718 (2005).

71. Hess, B. P-LINCS: A Parallel Linear Constraint Solver for Molecular Simulation. *J. Chem. Theory Comput.* **4**, 116–122 (2008).

72. Bussi, G., Donadio, D. & Parrinello, M. Canonical sampling through velocity rescaling. *J. Chem. Phys.* **126**, 014101 (2007).

73. Parrinello, M. & Rahman, A. Polymorphic transitions in single crystals: A new molecular dynamics method. *J. Appl. Phys.* **52**, 7182–7190 (1981).

74. Mohanram, H., Georges, T., Pervushin, K., Azaïs, T. & Miserez, A. Self-assembly of a barnacle cement protein (MrCP20) into adhesive nanofibrils with concomitant regulation of CaCO3 polymorphism. *Chem. Mater.* **33**, 9715–9724 (2021).

Author contributions

A.M. planned and supervised the project. M.H.B. and S.H.H. contributed equally to this work. A.M., M.H.B. and S.H.H. conceived the experimental design. M.H.B. expressed and purified rMrCP20 for all experiments. S.H.H. performed the FESEM, EDX, FTIR-ATR, and nanoindentation measurements. M.H.B. carried out the anticorrosion tests (ICP-OES, EIS, PDP, CV measurements) and QCM-D. T.S. conducted XPS and AES measurements. W.G.S. performed and analyzed SAXS experiments. G.G. validated data analysis of SAXS studies. R.W. advised on electrochemical studies and validated their data interpretation. Y.M. conducted MD simulation. M.H.B., S.H.H., and A.M. wrote the manuscript. All authors contributed to the discussion and editing of the manuscript.

Competing interests

The authors declare no competing interests.

Additional information

Supplementary information The online version contains supplementary material available at https://doi.org/10.1038/s43246-024-00445-z.

Correspondence and requests for materials should be addressed to Ali Miserez.

Peer review information *Communications Materials* thanks the anonymous reviewers for their contribution to the peer review of this work. Primary Handling Editors: Jet-Sing Lee. A peer review file is available.

Reprints and permission information is available at http://www.nature.com/reprints

Publisher's note Springer Nature remains neutral with regard to jurisdictional claims in published maps and institutional affiliations.